Appendix A

Theoretical analysis of Kerr-nonlinearity parametric oscillation in a whispering-gallery microcavity

A.1 Introduction

This section complements the discussion of the Kerr nonlinearity parametric oscillation in a microcavity as presented in chapter 10. Starting from the classical equations of four-wave-interaction for plane waves, the equations for parametric interaction in a microcavity are derived. The treatment in the case for optical modes of a resonator will lead to identical coupled-wave-equations, however with modified coupling coefficients. These coupling coefficients are determined by the pump, signal and idler overlap factors.

A.2 Third order nonlinear polarization

The nonlinear Polarization can be introduced phenomenologically by expanding the polarization in terms of the electric field. In the case of Kerr-nonlinear interaction, the 2^{nd} order nonlinearity is not present due to inversion symmetry, such that the

first nonlinear contribution is third order:

$$P_i = \chi E_i + \chi^{(3)}_{ijkl} E_i E_j E_k + ...$$

The physical process underlying the third order nonlinearity is a four-photon interaction. For the present treatment, it is assumed that the two pump fields are frequency degenerate. Inserting four fields and their amplitudes E_p ,(E_p), E_s, E_i into the above equation (i.e. $E_p(t) = \frac{1}{2} E_p e^{i\omega_p t} + c.c.$) for the nonlinear polarization, and neglecting anti-resonant terms such as $E_p E_p E_p \propto e^{-3i\omega_p t}$ (i.e. using the rotating wave approximation) several nonlinear optical terms can be identified, which lead to the generation of new frequency components, as well as phase shifts.

The phase insensitive terms $\propto |E_i|^2 E_j$ give rise to a change in the index of refraction n the field experiences and are referred to as *self-phase modulation(SPM)*, and *cross-phase modulation (XPM).* The change of index is related to then nonlinear index of refraction by: $n = n_0 + I \cdot n_2$[1]. As the name implies SPM refers to the change in index induced by the field itself, whereas XPM refers to the situation where the index of refraction is modified by the presence of a different field.

The phase sensitive polarization terms, such as $E_i E_i E_j^*$ (where $i \neq j$), give rise to parametric frequency conversion. In a classical picture this process can be viewed as being due to the temporal modulation of the refractive index $n(t) = n_0 + \Delta n_2(t)$ due the beat-frequency caused by two fields at different frequencies. Whereas the spatial modulation of the refractive index, gives rise to Bragg reflection, the temporal modulation of the refractive index gives rise to a frequency shift. The governing equations of motion are particularly simple for plane waves, assuming:

$$\begin{aligned} \vec{E}(r,t) &= \frac{1}{2} E(z) \exp(i(\omega t - kz)) + c.c \\ \vec{P}(r,t) &= \frac{1}{2} P(z) \exp(i(\omega t - kz)) + c.c \end{aligned}$$

[1]Some authors also define the nonlinear index of refraction as: $n = n_0 + n_2 \left|\vec{E}\right|^2$.

Susceptibility expression	Associated Nonlinear Optical Processes
$\chi^{(3)}_{\mathrm{Re}}\ E_i \left\|E_i\right\|^2$	Self-phase modulation (SPM)
$\chi^{(3)}_{\mathrm{Re}}\ E_i \left\|E_j\right\|^2$	Cross-phase modulation (XPM)
$\chi^{(3)}_{\mathrm{Re}}\ E_i E_i E_j^*, ...$	Four wave mixing process (FWM)
$\chi^{(3)}_{\mathrm{Im}}\ E_i \left\|E_i\right\|^2$	two-photon absorption
$\chi^{(3)}_{\mathrm{Im}}\ E_i \left\|E_j\right\|^2$	Raman-process (Stokes gain,...)
$\chi^{(3)}_{\mathrm{Im}}\ E_i E_i E_j^*, ...$	coherent anti-stokes Raman scattering

Table A.1: Nonlinear optical effects associated with the third-order susceptibility

the governing equations for four-wave mixing are given by [91][93]:

$$\begin{aligned}
\frac{\partial E_p}{\partial z} &= \left(\frac{i\omega_p}{c}\right)\frac{3}{8}\chi^{(3)}_{\mathrm{Re}}\left(E_p^2E_p^* + 2E_pE_iE_i^* + 2E_pE_sE_s^* + 4E_sE_pE_p^* + 2E_pE_pE_i^*\right)\\
\frac{\partial E_s}{\partial z} &= \left(\frac{i\omega_s}{c}\right)\frac{3}{8}\chi^{(3)}_{\mathrm{Re}}\left(E_s^2E_s^* + 2E_sE_iE_i^* + 4E_sE_pE_p^* + 2E_pE_pE_i^*\right)\\
\frac{\partial E_i}{\partial z} &= \left(\frac{-i\omega_i}{c}\right)\frac{3}{8}\chi^{(3)}_{\mathrm{Re}}\left(\underbrace{fE_i^{\,2}\left|E_i\right|}_{\text{SPM}} + \underbrace{2fE_i\left|E_s\right|^2}_{\text{XPM (Idler)}} + \underbrace{4fE_i\left|E_p\right|^2}_{\text{XPM(Pump)}} + \underbrace{2fE_pE_pE_s^*}_{\text{FWM-Term}}\right)
\end{aligned}$$

If one assumes that the pump field is not depleted, and that the signal and idler fields are weak, the coupled mode equations simplify considerably:

$$\begin{aligned}
\frac{\partial E_p}{\partial z} &= \left(\frac{i\omega_p}{c}\right)\frac{3}{8}\chi^{(3)}_{\mathrm{Re}}\left(E_p^2E_p^* + 4E_sE_pE_p^* + 4E_pE_pE_i^*\right)\\
\frac{\partial E_s}{\partial z} &= \left(\frac{i\omega_s}{c\epsilon_0}\right)\frac{3}{8}\chi^{(3)}_{\mathrm{Re}}\left(4fE_s\left|E_p\right|^2 + 2fE_pE_pE_i^*\right)\\
\frac{\partial E_i}{\partial z} &= \left(\frac{-i\omega_i}{c\epsilon_0}\right)\frac{3}{8}\chi^{(3)}_{\mathrm{Re}}\left(4fE_i\left|E_p\right|^2 + 2fE_pE_pE_s^*\right)
\end{aligned}$$

A.3 Coupled mode equations for Kerr-parametric interactions in a whispering-gallery-microcavity

To formulate the coupled mode equations for Kerr oscillations in a cavity, the governing equations are first formulated in the temporal domain, and cavity losses and

pumping via a waveguide are introduced using the previously introduced formalism. Starting point for the derivation of the coupled mode equations is the wave-equation:

$$\left(-\nabla^2 + \frac{n^2}{c^2}\frac{\partial^2}{\partial t^2}\right)\overrightarrow{E} = \mu_0 \frac{\partial^2}{\partial t^2}\overrightarrow{P}_{NL}$$

To derive an equation for the coupled amplitudes of the whispering-gallery waves, the Helmholtz equation is first solved for the case of a whispering gallery mode of the system (i.e. the homogeneous solution, without the nonlinear polarization term). The general form of a whispering gallery mode, expressed in cylindrical coordinates for the case of a TM mode is:

$$E_z^i(r,z,\phi,t) = \frac{1}{2}E_z^i(r,z)e^{i\ell_i\phi + i\omega t} + c.c.$$

Here ℓ is the angular mode number of the whispering gallery mode. Due to the presence of the nonlinear polarization the whispering gallery modes will exhibit an additional time dependence, expressing the fact that fields might be created, or absorbed. To describe the growth of the WGM the amplitude is introduced, which only depends on the time,

$$E_z^i(r,z,\phi,t) = \frac{1}{2}A^i(t)\cdot E_z^i(r,z)e^{i\ell_i\phi + i\omega t} + c.c$$

The effect of the nonlinear polarization can now be investigated, by deriving a coupled mode equation for the field amplitude $A^i(t)$:

$$\left(-\nabla^2 + \frac{n^2}{c^2}\frac{\partial^2}{\partial t^2}\right)A^i(t)\cdot E_z^i(r,z)e^{i\ell_i\phi + i\omega t} = \mu_0 \frac{\partial^2}{\partial t^2}\overrightarrow{P}_{NL}$$

$$A^i(t)\cdot\underbrace{\left(-\nabla^2 + \frac{n^2}{c^2}\frac{\partial^2}{\partial t^2}\right)E_z^i(r,z)e^{i\ell_i\phi + i\omega_i t}}_{=0} + \left(\frac{n^2}{c^2}\frac{\partial^2 A^i(t)}{\partial t^2} + 2i\omega\frac{n^2}{c^2}\frac{\partial A^i(t)}{\partial t}\right)E_z^i(r,z)e^{i\ell_i\phi + i\omega_i t} = \mu_0\frac{\partial^2}{\partial t^2}\overrightarrow{P}_{N}$$

The first term on the right hand side is zero, since E is assumed to be a mode i.e. a solution of the homogenous problem. To arrive at a coupled wave equation, the slowly varying amplitude approximation can be made, i.e. assuming:

$$\left|\frac{\partial^2 A^i(t)}{\partial t^2}\right| \ll \left|2i\omega_i \frac{\partial A^i(t)}{\partial t}\right|$$

leading to:

$$\left(2i\omega_i \frac{n^2}{c^2}\frac{\partial A^i(t)}{\partial t}\right) E_z^i(r,z)e^{i\ell_i\phi + i\omega_i t} = \mu_0 \frac{\partial^2}{\partial t^2}\overrightarrow{P}_{NL}$$

This is a good approximation, since the conversion due to nonlinear optical processes is slow compared to the time-scale of the optical cycle ω. Next, the polarization term has to be re-casted:

$$\frac{\partial^2}{\partial t^2}\overrightarrow{P}_{NL} = \frac{\partial^2}{\partial t^2}\left(\chi_{ijk}E_jE_kE_l\right)$$

The nonlinear susceptibility has been treated in the last section. The product of the three whispering-gallery mode fields on the l.h.s. contains a rapidly varying term (due to the phase of the whispering-gallery modes $\propto\ e^{i\omega_i t}$), and a slowly varying part (given by the amplitude $A(t)$). In taking their derivative with respect to time, the slow time dependence of the fields can be neglected. Assuming that the total three fields vary as $E_iE_jE_k \propto e^{i(\omega i+\omega_j+\omega_k)t} \equiv e^{i\omega' t}$

$$\mu_0\frac{\partial^2}{\partial t^2}\overrightarrow{P}_{NL} = \mu_0\omega'^2\left(\chi_{ijkl}E_jE_kE_l\right)$$

In addition each of the field contains a azimuthal dependence due to the eigenfunctions $exp(\pm i\ell\phi)$. Therefore the polarization also contains a term:

$$E_iE_jE_k \propto e^{i(li+l_j+l_k)\phi}$$

Inserting the phasor and angular dependence into the polarization leads to:

$$\left(2i\omega_i\frac{n^2}{c^2}\frac{\partial A^i(t)}{\partial t}\right)\widetilde{E}^i_z(r,z)e^{i\ell_i\phi+i\omega_i t} = \mu_0\omega_i'^2\left(\frac{3}{8}\chi_{ijk}\widetilde{E}_j\widetilde{E}_k\widetilde{E}_l A_j A_k A_l\right)e^{i(\omega j+\omega k+\omega_l)t}e^{i(\ell j+\ell k+\ell_l)\phi}$$

$$\left(\frac{\partial A^i(t)}{\partial t}\right)\widetilde{E}^i_z = -\frac{i\omega_i'^2}{2\epsilon_o n^2\omega_i}\left(\frac{3}{8}\chi_{ijk}\widetilde{E}_j\widetilde{E}_k\widetilde{E}_l A_j A_k A_l\right)e^{i(\omega j+\omega k+\omega_l-\omega i)t}e^{i(\ell j+\ell k+\ell_l-$$

The latter equation is cumbersome to evaluate, since the explicit fields $\widetilde{E}_i = \widetilde{E}_i(r,z)$ enter in the equation. It is desirable to arrive at an equation which describes only the energy or amplitude of the mode i.e. $A(z)$. This can be achieved by integrating over the transverse extend of the WG mode and by multiplying the conjugate field $\widetilde{E}^i_z(r,z)^*$ from the left.

$$\left(\frac{\partial A^i(t)}{\partial t}\right)\int_{r,z}\left|\widetilde{E}^i_z\right|dA = -\frac{3}{8}\frac{i\omega_i'^2}{2\epsilon_o n^2\omega_i}\left(\chi_{ijk}\widetilde{E}_i\widetilde{E}_j\widetilde{E}_k A_i A_j A_k\right)e^{i(\omega j+\omega k+\omega_l-\omega i)t}e^{i(\ell j+\ell k+\ell_l-\ell i)\phi}$$

$$\left(\frac{\partial A^i(t)}{\partial t}\right) = -\frac{3}{8}\frac{i\omega_i'^2}{2\epsilon_o n^2\omega_i}\chi_{ijk}A_i A_j A_k\cdot\underbrace{\left(\int_{r,z}\widetilde{E}_i\widetilde{E}_j\widetilde{E}^*_k\widetilde{E}^{i*}_z\,dA\right)}_{\equiv A^{-1}_{eff}}e^{i(\omega j+\omega k+\omega_l-\omega i)t}e^{i(\ell j+\ell k+\ell_l}$$

In the last expression, the fact that the mode function are normalized has been used, i.e. $\int_{r,z}|E_i|^2\,dA = 1$. The last term is the effective mode area and has units of inverse area, which as in the case of Raman scattering deviates from the mode area, as defined by the energy density definition. In the case E is describes the electric field and is not normalized, the effective area is given by:

$$A^{-1}_{eff} \equiv f_{ijkl} = \frac{\int_{Acav}E^*_i E^*_j E_k E_l dA}{\prod\limits_i\left(\int_A|E_i|^2\,dA\right)^{1/2}}$$

Since in a microcavity the susceptibility vanishes outside the cavity (i.e. in air) the integral in the denominator is carried out only over the dielectric cavity area). As in the case of stimulated Raman scattering, the effective mode area can actually differ from the actual mode area (and for microspheres and microtoroids is approximately $\times 2$ larger). The above definition of effective mode area describes all third order nonlinear optical phenomena, and as such also yields again the Raman gain coefficient

(i.e. which is proportional to $P \propto E_i^* E_i^* E_k$ i.e. yielding $A_{eff}^{-1} = A_{ppss.}$). Hence the coupled mode equations are given by:

$$\left(\frac{\partial A^i(t)}{\partial t}\right) = -\frac{i\omega_i'^2}{2\epsilon_o n^2 \omega} f_{ijkl} \cdot \frac{3}{8}\chi^{(3)}_{ijk} \cdot A_j A_k A_l e^{i(\omega j + \omega k + \omega_l - \omega i)t} e^{i(\ell j + \ell k + \ell_l - \ell i)\phi}$$

Furthermore it is common to introduce the nonlinear coefficient:

$$\gamma_i \equiv \frac{n_2 \omega_i}{c} f_{ijkl} \approx \frac{n_2 \omega_i}{c A_{eff}}$$

Where the third order nonlinear susceptibility is related to the nonlinear index of refraction n_2 by, and A_{eff} is assumed to identical for all coupling processes.

$$n_2 = \frac{3}{8n}\chi^{(3)}$$

The fields entering the expression of the nonlinear polarization can only couple to the l.h.s. of the Helmholtz equation, if the time dependence is the same as on the left, i.e. if $P \propto e^{i\omega_i t}$. The remaining terms are anti-resonant (and in a full quantum mechanical treatment are seen to violate energy conservation with respect to the photon energy). Therefore only terms, in which $\omega_i \approx \omega'$ will induce an efficient coupling by means of the nonlinear susceptibility. In addition the angular dependence $e^{il\phi}$ on both sides of the equation needs to be identical, to achieve coupling of modes. The latter two conditions, can be shown to be equivalent to the requirement of energy and angular momentum conservation. To arrive at a set of coupled mode equations for parametric oscillation, which parametrically converts two pump photons into signal and idler, only resonant terms have to be kept in the treatment. For i, j, k, l equal to two pump fields, as well as signal and idler, this leads to the coupled mode equations for signal

and idler.

$$\begin{aligned}
\frac{\partial A_p}{\partial t} &= i\left(\frac{c}{n}\right)\frac{n_2\omega_p}{2cA_{eff}}\left(A_p\left|A_p\right|^2 + 4A_pA_pA_{si}^{**}e^{i\Delta\omega t}e^{i\Delta l\phi} + 4A_pA_pA_i^{*}e^{i\Delta\omega t}e^{i\Delta l\phi}\right)\\
\frac{\partial A_s}{\partial t} &= i\left(\frac{c}{n}\right)\frac{n_2\omega_s}{2cA_{eff}}\left(4A_s\left|A_p\right|^2 + 2A_pA_pA_i^{*}e^{-i\Delta\omega t}e^{-i\Delta l\phi}\right)\\
\frac{\partial A_i}{\partial t} &= i\left(\frac{c}{n}\right)\frac{n_2\omega_i}{2cA_{eff}}\left(4A_i\left|A_p\right|^2 + 2A_pA_pA_s^{*}e^{-i\Delta\omega t}e^{-i\Delta l\phi}\right)
\end{aligned}$$

In this set of equations, the pump has been assumed strong $|A_p| \gg |A_i|, |A_s|$, and for the idler and signal only the XPM and FWM term included, whereas the pump field experiences only SPM and FWM to signal and idler frequencies. In addition the angular momentum and frequency detuning parameters have been introduced:

$$\begin{aligned}
\Delta\omega &\equiv 2\omega_p - \omega_I - \omega_S\\
\Delta\ell &= 2\ell_p - \ell_i - \ell_S
\end{aligned}$$

(Angular) Momentum conservation for WGM

It is important to note, that if the signal and idler mode numbers are chosen symmetrically around the pump field, the (angular) momentum matching condition is satisfied intrinsically (since $\beta = \frac{\ell}{R_0}$):

$$\beta_\ell + \beta_\ell + \beta_{\ell+N} + \beta_{\ell-N} = 0$$

Energy conservation

On the other hand, energy conservation is not a priori assumed to be satisfied, due to the presence of waveguide and material dispersion. The detuning $\Delta\omega$ effectively describes the extent to which strict energy conservation is violated and is given by:

$$\Delta\omega \equiv 2\omega_p - \omega_I - \omega_S$$

It is interesting to note, in the case of a cavity, the role of frequency and momentum in the context of parametric gain are reversed. In the waveguide case, a continuum of

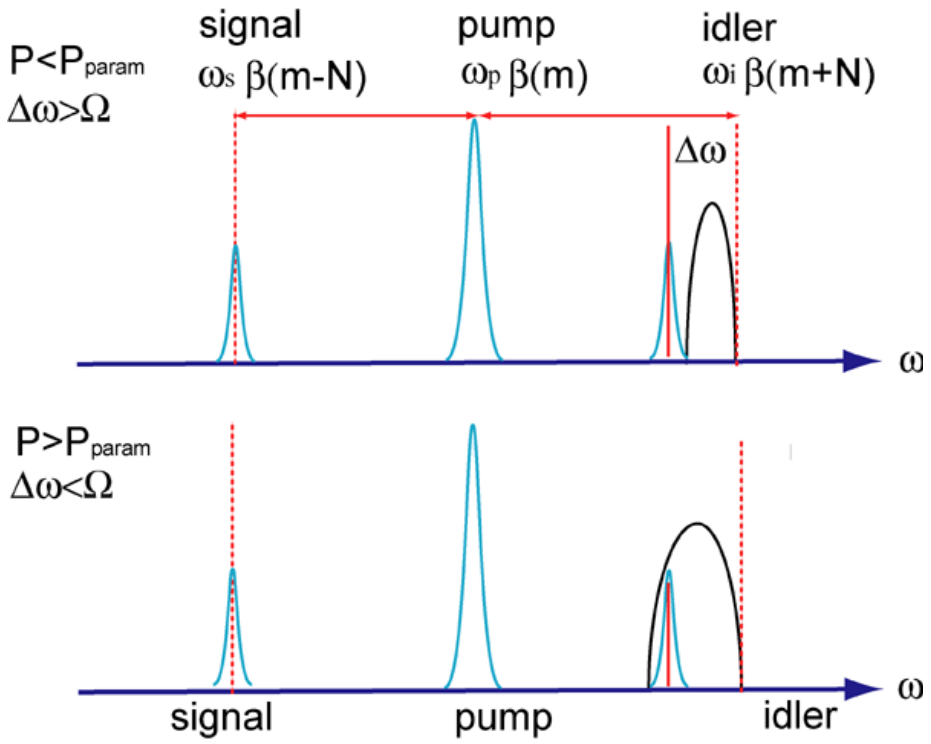

Figure A.1: Schematic of the effect of cavity detuning on the occurrence of parametric oscillation. For $\Delta\omega > 0$, parametric oscillation can only occur if the detuning $\Delta\omega = 2\omega_p - \omega_s - \omega_i$ is less than the parametric band-width (given by $0 < \Delta\omega < \Omega$).Note that the parametric band-width exists only for positive detuning, due to the shift of resonant frequency caused by XPM and SPM.

frequencies ω exists, such that energy conservation is a priori satisfied, whereas the momentum distribution is discrete $\overrightarrow{k_i}(\omega)$. In contrast, for a whispering-gallery microcavity, momentum is satisfied intrinsically, whereas only a discrete set of frequencies exist $\omega_{n\ell mp}$, which are required to satisfy energy conservation. Using the frequency detuning, the coupled-mode-equations are:

$$\begin{aligned}\frac{\partial A_s}{\partial t} &= -\frac{1}{2\tau_s}A_s + i\kappa_1 A_s + i\kappa A_i^* e^{i\Delta\omega t} \\ \frac{\partial A_i}{\partial t} &= -\frac{1}{2\tau_i}A_i - i\kappa_1 A_i - i\kappa A_s^* e^{i\Delta\omega t}\end{aligned}$$

Where:

$$\begin{aligned}\kappa_1 &\equiv \left(\frac{\omega_p}{c}\right)\frac{3}{8}\chi^{(3)}4f\left|A_p\right|^2 = 4\left|A_p\right|^2\gamma \\ \kappa &\equiv \left(\frac{\omega_p}{c}\right)\frac{3}{8}\chi^{(3)}2fA_pA_p = 2A_pA_p\gamma\end{aligned}$$

In the case of a whispering-gallery microcavity, the governing equation for the pump whispering gallery mode is given by the equation:

$$\begin{aligned}\frac{\partial \widetilde{A}_p}{\partial t} &= -\frac{1}{2\tau_p}A_p + i\kappa_{sp}A_p + \kappa_{kp}A_p^* e^{-i\Delta\omega t} + \sqrt{\frac{1}{\tau_{ex}}}s \\ \kappa_{kp} &\equiv \frac{3}{8}\chi^{(3)}f\cdot 2A_sA_i \\ \kappa_{sp} &\equiv \frac{3}{8}\chi^{(3)}f\cdot\left|A_p\right|^2\end{aligned}$$

This set of equations of coupled equations for signal and idler fields can be formally solved. By the transforming into a rotating frame i.e. $A_s = A_s e^{-i\Delta\omega t/2}$, $A_I = A_I e^{-i\Delta\omega t/2}$ and eliminating the time dependence yields the linear system of coupled equations:

$$\begin{aligned}\frac{\partial A_s}{\partial t}e^{-i\frac{\Delta\omega}{2}t} - i\frac{\Delta\omega}{2}A_s e^{-i\frac{\Delta\omega}{2}t} &= -\frac{1}{2\tau_s}A_s e^{-i\frac{\Delta\omega}{2}t} + i\kappa_1 A e^{-i\frac{\Delta\omega}{2}t} + i\kappa A_i^* e^{+i\Delta\omega t/2} \\ \frac{\partial A_i}{\partial t}e^{-i\frac{\Delta\omega t}{2}} - i\frac{\Delta\omega}{2}A_I e^{-i\frac{\Delta\omega t}{2}} &= -\frac{1}{2\tau_i}A_i e^{-i\frac{\Delta\omega}{2}t} - i\kappa_1 A_i e^{-i\frac{\Delta\omega}{2}t} - i\kappa A_s^* e^{+i\Delta\omega t/2}\end{aligned}$$

If the idler equation is conjugated a linear differential equation system is obtained:

$$\frac{\partial}{\partial t}\begin{pmatrix} A_s \\ A_i^* \end{pmatrix} = \begin{pmatrix} -\frac{1}{2\tau} + i\kappa_1 + i\frac{\Delta\omega}{2} & i\kappa \\ -i\kappa^* & -\frac{1}{2\tau} - i\frac{\Delta\omega}{2} - i\kappa_1 \end{pmatrix} \begin{pmatrix} A_s \\ A_i^* \end{pmatrix} \tag{A.1}$$

The eigenvalues are given by: $\lambda_{1,2} = \left\{ \pm \left(\frac{1}{2\tau} - \sqrt{|\kappa|^2 - \kappa_1^2 - \Delta\omega\kappa_1 - \frac{\Delta\omega^2}{4}} \right) \right\}$ and the parametric gain be identified correspondingly as:

$$\begin{aligned} g_{Param}(\Delta\omega) &= \sqrt{\left(\gamma |E_p|^2\right)^2 - \left(\gamma |E_p|^2 + \frac{\Delta\omega}{2}\right)^2} \\ &= \sqrt{2\gamma |E_p|^2 \Delta\omega - \frac{\Delta\omega^2}{4}} \end{aligned} \tag{A.2}$$

The parametric gain is non-zero only for $0 < \Delta\omega < \Omega_p$ where Ω_p is the parametric gain bandwidth:

$$\Omega_p \equiv 4\gamma |E_p|^2 \tag{A.3}$$

The maximum parametric occurs shifted away from ideal energy conservation, at non-zero detuning:

$$\Delta\omega_{\max} \equiv 2\gamma |E_p|^2 \tag{A.4}$$

This shift is due to the effect of cross phase modulation of the signal and idler due to the pump.

A.4 Parametric oscillation threshold

The parametric oscillation threshold is reached when the gain exceeds the cavity losses i.e. in steady state for $\lambda_{1,2} = 0$.Thus:

$$\sqrt{2\gamma |E_p|^2 \Delta\omega - \left(\frac{\Delta\omega}{2}\right)^2} = \left(\frac{1}{2\tau_0} + \frac{1}{2\tau_{ex}}\right) = \frac{1}{2\tau_0}(1+K) \tag{A.5}$$

From this equation the necessary circulating pump power in the cavity can be derived:

$$|E_p|^2 = \frac{\left(\frac{1}{2\tau_0}(1+K)\right)^2 + \left(\frac{\Delta\omega}{2}\right)^2}{2\gamma\Delta\omega} \tag{A.6}$$

Taking into account the cavity buildup factor, the threshold for parametric oscillation as a function of coupling and detuning is obtained:

$$P_t^{Kerr} = \frac{\omega_0^2 Q_0^{-2}(1+K)^2 + (\Delta\omega/2)^2}{2\gamma\Delta\omega \cdot \frac{c}{n_{eff}}} \left(\frac{\pi^2 R n_{eff}}{C(\Gamma)\lambda_0}\frac{(K+1)^2}{Q_0 K}\right) \tag{A.7}$$

$$\gamma \equiv \frac{n_2\omega_i}{cA_{eff}} \tag{A.8}$$

A.5 Material and cavity mode dispersion

The optical modes within a cavity are in general not regularly spaced due to the presence of material and cavity dispersion. First, material dispersion is considered. The detuning frequency can be related to $n' = \frac{dn}{d\omega}$ by noting that $\omega_i = \ell\lambda_i/2\pi R n_{eff}$ and in a simple model $n_{eff} \approx n(\omega)$.

$$\begin{aligned}
\Delta\omega &= \frac{c}{R}\left(\frac{2\ell_p}{n(\omega_p)} - \frac{\ell_s}{n(\omega_s)} - \frac{\ell_I}{n(\omega_I)}\right) \\
&= \frac{c}{R}\left(\frac{2\ell_p}{n(\omega_p)} - \frac{\ell_p - N}{n(\omega_p) - n'\Delta\omega} - \frac{\ell_p + N}{n(\omega_p) + n'\Delta\omega}\right), n' \equiv \frac{dn(\omega)}{d\omega}|_{\omega_p} \\
&= \frac{c}{R}\left(\frac{2\ell_p}{n(\omega_p)} - \frac{\ell_p}{n(\omega_p) - n'\Delta\omega} - \frac{\ell_p}{n(\omega_p) + n'\Delta\omega} + \frac{N}{n(\omega_p) - n'\Delta\omega} - \frac{N}{n(\omega_p) + n'\Delta\omega}\right) \\
&= \frac{c}{R}\left(\frac{\ell_p}{n(\omega_p)}\underbrace{\left[2 - 1 + \frac{n'}{n(\omega_p)}\Delta\omega - 1 - \frac{n'}{n(\omega_p)}\Delta\omega\right]}_{=0} + \frac{N}{n(\omega_p)}\left[1 + \frac{n'\Delta\omega}{n(\omega_p)} - 1 - \frac{n'\Delta\omega}{n(\omega_p)}\right]\right) \\
&= \frac{c}{R} 2N \frac{n'}{n(\omega_p)^2}\Delta\omega
\end{aligned}$$

In the case of silica in the 1550 nm band$\frac{dn}{d\omega} > 0$. Therefore the parametric detuning frequency due to material dispersion is always positive, as is required in order for parametric oscillation to occur. Secondarily, the free-spectral range is naturally not constant. In the case of a microsphere, the analysis of chapter 1 yielded:

$$\Delta\omega_{FSR} \equiv |\omega_{nm\ell} - \omega_{nm\ell+1}| \underset{\ell\gg 1}{\approx} \frac{c}{n_a R}\left(\frac{1}{m} - t_n^0 \frac{\ell^{-2/3}}{3}\right) \tag{A.9}$$

Therefore the detuning frequency contribution from the WGM dispersion is always positive, since the FSR ($\Delta\omega_{FSR}$) increases for increasing angular mode number ℓ.

$$\Delta\omega = 2\omega_p - \omega_i - \omega_S = \Delta\omega_{FSR}^{p-i} - \Delta\omega_{FSR}^{p-s}$$

As a result both material dispersion and cavity mode dispersion, cause the parametric detuning frequency to be $\Delta\omega > 0$.

Appendix B

Modelling of whispering-gallery microcavity modes

B.1 Wave equation for whispering-gallery resonators with rotational symmetry

Whereas the optical quality factor (Q) is dependent upon many external factors (such as cavity surface roughness, water adsorption, defects in the oxide layer etc.), and can vary significantly across micro-spheres and micro-cavities with nearly-identical geometry parameters, the mode volume of the optical modes is entirely dependent upon the cavity geometry. However, while Q-factor can be measured directly and is experimentally accessible, the same is not true for the optical mode volume, which can only be probed indirectly, such as by near field optical probes or as be presented in chapter 7, using the oscillation threshold of stimulated Raman scattering. In this section the optical mode-volumes as well as the effective nonlinear optical mode volumes are calculated for toroid and disk microcavities using numerical modelling using a PDE finite-element solver. To accomplish this task the Helmholtz equation for the whipering-gallery resonator case is derived and transformed in the required standard PDE form.

The whispering gallery resonators studied in this thesis (i.e. spheres, disks and toroids) all exhibit (if the presence of eccentricity is neglected, and only treated

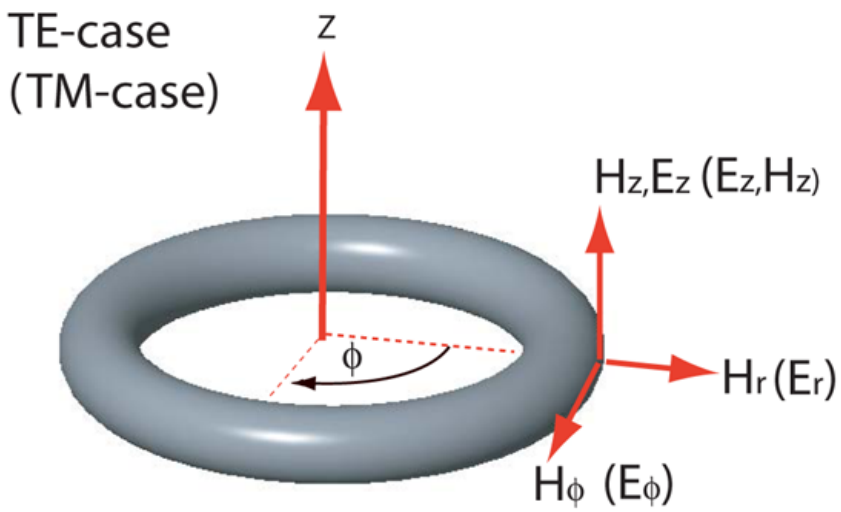

Figure B.1: Direction of the field components of the whispering-gallery modes of magnetic type (i.e.TE-case) for a toroid. TE (TM) modes posses a E-field (H-field) which is perpendicular to the equatorial plane of the torus.

as a weak pertubation) a rotational symmetry. Therefore the choice of cylindrical coordinates for the modelling is a natural choice. The optical modes of a whispering gallery type resonator are described in their most general form by a total of six field components, $(H_r, H_{\phi,} H_z, E_r, E_{\phi,} E_z)$. The boundary condition couples the electric and magnetic field components. A significant simplification occurs, if the index of refraction $n(r)$ is homogeneous throughout the dielectric cavity, and the polarization is constant. In this case the scalar-wave equation approximation can be used. The solutions of the scalar wave equation fall into two classes; the optical modes are either electric in character (referred to as transverse-magnetic TM case) or magnetic in character (referred to as transverse electric TE case). In the case of TM-modes in a WGM resonator (with the symmetry axis along the z-axis) , the magnetic field is transverse to the direction of propagation (which occurs along $\overrightarrow{e}_\phi$) implying that $H_\phi = 0$, whereas for the TE-case $E_\phi = 0$. All the remaining field components can be expressed in terms by only one field component (H_ϕ for TE-modes and E_ϕ TM-

modes) , reducing the problem to a scalar Helmholtz equation for one field component. An additional simplification of the Helmholtz equation occurs due to the rotational symmetry in case of a perfect whipering-gallery resonator. Due to the periodicity condition ($\exp(-\beta_l 2\pi) = 1$) the TE and TM-mode can be expressed as:

$$\left\{ \begin{array}{c} E_\phi(r,z,\phi) \\ H_\phi(r,z,\phi) \end{array} \right\} = \left\{ \begin{array}{c} E_\phi(r,z) \\ H_\phi(r,z) \end{array} \right\} \cdot \exp(i([\pm\beta\phi - \omega t])and\beta_l = l \tag{B.1}$$

Where l is the angular mode number. The Helmholtz in cylindrical coordinates is given by (considering in what follows only the TM case):

$$(\overline{\nabla}^2 + \frac{\omega^2}{c^2}n^2)E_\phi = \left[\left(\frac{d^2}{dr^2} + \frac{1}{r}\frac{d}{dr}\right) + \frac{1}{r^2}\frac{d^2}{d\phi^2} + \frac{d^2}{dz^2} + \frac{\omega^2}{c^2}n^2\right] E_\phi = 0 \tag{B.2}$$

Using the separation of variables approach for the angular direction (and introducing the angular mode l number correspondingly):

$$E_\phi(r,z,\phi) = E_\phi(r,z) \cdot \exp(\pm il\phi) \tag{B.3}$$

this yields the equation:

$$\left[\left(\frac{d^2}{dr^2} + \frac{1}{r}\frac{d}{dr}\right) - \frac{1}{r^2}l^2 + \frac{d^2}{dz^2} + \frac{\omega^2}{c^2}n^2\right] E_\phi = 0 \tag{B.4}$$

multiply by $r\cdot$ from the left and rearranging:

$$\begin{aligned} \left[\left(r\frac{d^2}{dr^2} + \frac{d}{dr}\right) + r\frac{d^2}{dz^2} - \frac{1}{r}l^2 + r\frac{\omega^2}{c^2}n^2\right] E_\phi &= 0 \\ \frac{d}{dr}\left(r\frac{d}{dr}E_\phi\right) + \frac{d^2}{dz^2}\left(rE_\phi\right) - \left(\frac{1}{r^2}\mathbf{l}^2 - \frac{\omega^2}{c^2}\mathbf{n}^2\right) rE_\phi &= 0 \end{aligned}$$

Rearranging and the expression thus produces the Helmholtz equation in the required PDE format (TM -case):

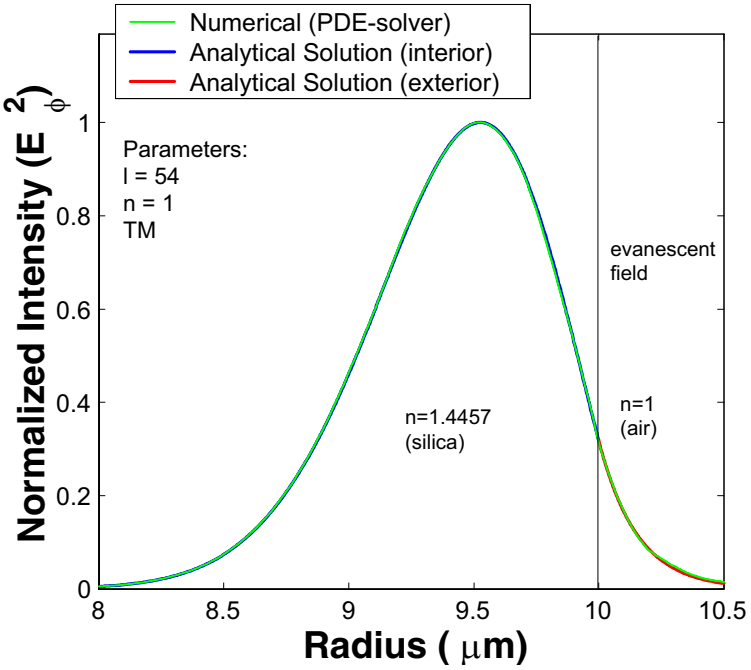

Figure B.2: Comparisson of the analytical and numerically calculated intensity distribution of the $|E_\phi|^2$ component plotted in the radial direction, for a microsphere of 10 μm radius.The numerical and analytical models show excellent agreement.

$$\begin{aligned} \overline{\nabla}_{r,z}\cdot(\mathbf{r}\overline{\nabla}_{r,z}\mathbf{E}_\phi)+\left(\frac{\omega^2}{c^2}n^2-\frac{l^2}{r^2}\right)\mathbf{r}\mathbf{E}_\phi &= \mathbf{0} \\ -\overline{\nabla}_{r,z}\cdot(\mathbf{r}\overline{\nabla}_{r,z}\mathbf{E}_\phi)+\frac{\beta^2}{r}\mathbf{E}_\phi &= \frac{\omega^2}{c^2}n^2\mathbf{r}\mathbf{E}_\phi \end{aligned} \tag{B.5}$$

To test the accuracy of the numerical modelling, the calculated resonance locations for a microsphere were compared to the resonance locations obtained by an asymptotic expansion (see chapter 1). The deviations were less than 2.5e-004 for both TE and TM polarization, and assure the accuracy of the simulation results. Furthermore, in figure B.2 the numerical and theoretical results of the radial equation are plotted, showing excellent agreement.

Appendix C

Experimental techniques: Fabrication of toroid and disk microcavities on a silicon chip

Surface-tension induced microcavities such as droplets of microspheres undergo a liquid phase, in which surface tension induces the spherical cavity shape and in addition provides exceptionally smooth surfaces. For silica microspheres, atomic-force microscopy has revealed surface roughness in the range of less than 1 nm r.m.s. The quality of the surface has enabled to observe absorption limited Q-factors in microspheres of nearly 9×10^9[41], which are the highest Q-factors to date in the optical domain. In this chapter the fabrication of toroidally shaped silica microcavities on a silicon chip is described. The fabrication technique is a combination of standard micro-fabrication techniques with a selective reflow process inherent to fabrication of surface-tension-induced microcavities. As in the case of microspheres, toroid microcavities undergo a liquid state during their fabrication, enabling them to obtain surface roughness characteristics similar to other surface-tension-induced microcavities such as microspheres. This allows, under proper preparation, to observe ultra-high-Q optical modes, as has been demonstrated in chapter 7, and constitutes the first demonstration of ultra-high-Q microcavity on a chip[81].

The fabrication sequence involves as a first step the fabrication of silica disk microcavities on a silicon substrate. Microdisk also fall into the class of whispering-gallery devices, as their modes are confined by continuous total internal reflection at the disk

perimeter. In a second step, the disk-cavities are laser irradiated causing a selective reflow of the silica. This process causes the disk surface to collapse and to from a toroidally shaped boundary, whose limiting dimensions are defined by the pillar geometry.

Starting material for the fabrication process are oxidized silicon wafers (in the work intrinsic oxidized wafers with resistivity of typically more than >10 Ohm/cm^2 and [100] crystal orientation, Virginia Semiconductors). Processing involved the etching of circular pads into the oxidized wafers. In this thesis work positive photo-resist (Shipley-1813) was used and spun for 2 minutes at 3000 rpm. To promote adhesion of the photo-resist the wafer was exposed to HDMS prior to spinning. After soft-bake (115 C at 2 minutes) the wafers were exposed and developed (MF-319), and hard-baked (120 C for 15 minutes). After visual inspection on the uniformity of the pads, the wafers were etched with hydrofluoric acid until all oxide was removed, leaving circular pads on a silicon wafer. Since silicon is hydrophilic as opposed to silica, the removal of the entire layer of oxide can be inferred visually. Due to the isotropy of the HF etching, combined with the effect of undercutting of the photo-resist, the silica disks exhibit wedge shaped side-wall profiles. The wedge angle is dependent on the amount of undercutting of the photo-resist pads and was less than 45 degree in this work. After etching the sample was cleaned with acetone, methanol and DI. Critical in the processing is avoiding particles during cleaving of the wafer into individual chips. This was achieved by spinning (and subsequently soft-baking) a second time photo-resist on the etched sample. The layer of photo-resist in this case functioned as a protection layer for particles during cleaving. The processed wafer was cleaved into ca. 5×20mm chips, in order to facilitate the coupling using tapered optical fibers. Each chip contained one single row of resonators, to ensure rapid testing of resonators. After cleaving individual chips containing the photo-resist layer were rinsed with water and all particles removed. Subsequently the samples were cleaned in acetone, at a temperature of 60 degrees for 15 minutes followed by a methanol and DI rinse. This ensured complete removal of the photo-resist. To optically isolate the silica disks from the silicon a dry (gas-) etch employing XeF_2 at

room temperature was used. Figure **??** shows a scanning electron micrograph of the resulting structure. The amount of undercut can be controlled by the XeF_2 etching parameters, however large variations were found at the edges of the samples, likely due to proximity and inhomogeneous gas-flow. The resulting structures are microdisk cavities, and their optical modes will be examined in chapter 7. Nonetheless, the above process flow leaves lithographic blemishes, visible in an optical microscope, at the all-important disk periphery. Therefore additional processing was pursued to achieve the surface finish characteristic of STIM structures exhibiting rms roughness of several nanometers or less[41].

Next, a processing step was introduced to selectively heat and reflow the undercut SiO_2disks without affecting the underlying silicon support pillar similar to techniques used for integrated circuit planarization[113]. This steps leaves toroidally shaped cavities with a surface roughness which is comparable to surface-tension induced microcavities such as microspheres. The reflow step was performed using a Carbon dioxide laser (Synradt Inc., 10W optical power), which was also used for the fabrication of microsphere resonators. The CO_2 laser emitted in a TEM_{00} mode and had a beam diameter of ca. 1 mm. Improved beam profiles were obtained when increasing the optical path length of the laser to the sample ca. 4 feet. The laser was focused using a 5 inch focal length lens (Umicore Inc.), resulting in a beam diameter of ca. 200 μm diameter. As during the reflow process alignment of the Gaussian laser beam with the silica disk is critical, a 45-degree ZeSn alignment beam-splitter with a 633 nm reflective coating was used. The beam-splitter was placed directly after the ZeSn lens and a $\times 20$ objective with a focal length of 6 cm was used to image the laser spot. The chips with the silica disks were mounted vertically on a sample holder mounted on a stage, to allow relative positioning with respect to the image and laser spot. The schematic of the setup is shown in C.1.

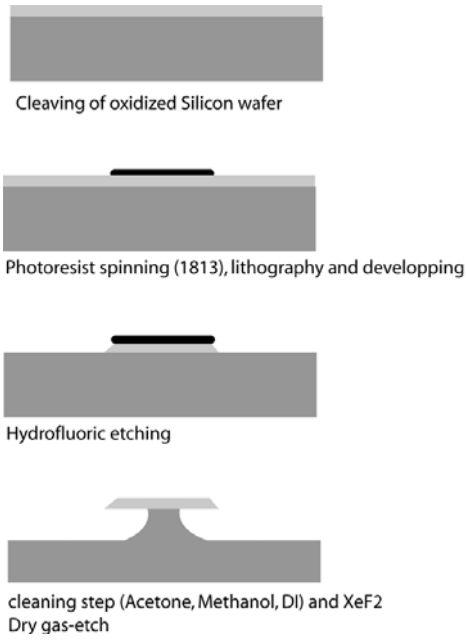

Figure C.1: Microcavity fabrication steps: 1. Cleaving 2. Photolithography 3. Wet-etching using hydrofluoric acid 4. Dry etching using XeF_2.

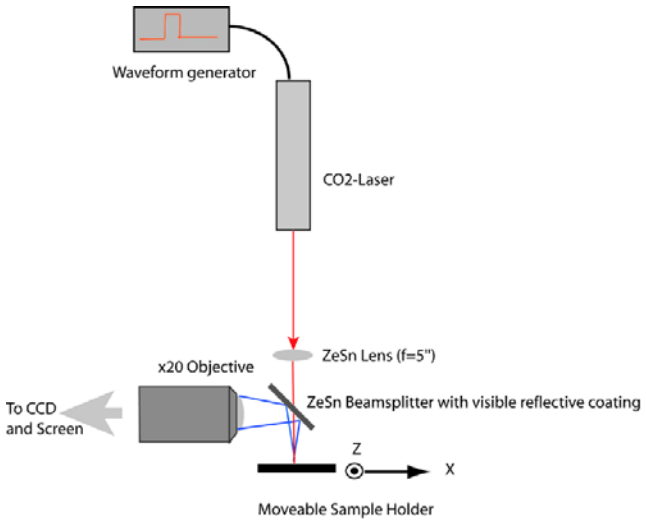

Figure C.2: Schematic of the CO_2-laser selective reflow process to create toroidally shaped microcavities.

C.1 Properties of Silica and Silicon at CO_2 laser wavelength

Silicon, due to its band-gap of 1.12 eV, does not absorb the energetically lower photons from the CO_2 laser (10.6 μm wavelength which corresponds to 0.12 eV) through direct optical excitation of valence band electrons. Heating and corresponding absorption is primarily caused by free-carrier-absorption (FCA) of thermally excited electrons in the conduction band. At room temperature silicon is therefore nearly transparent to CO_2 laser light. At higher temperature the silicon absorption increases through thermally excited carriers, which in turn increase the absorption due to free-carriers excitation. This positive feedback of the heating is referred to as thermal runaway heating. For the laser intensities in this work, thermal run-away heating of silicon was not observed, as the laser intensities were below 100 MW/cm^2.

Silica, on the contrary does strongly absorb CO_2 laser light due to the presence of resonant vibrational levels near 10.6 μm . Strong absorption occurs due to excitation of the transverse optical and longitudinal optical phonon mode of the $O-Si-O$ bond which is located at 1090 cm^{-1} and 1200 cm^{-1} respectively. The room temperature absorption coefficient is 32 inverse micron. For higher temperature the silica absorption increases to a good degree linearly due to thermal run-away. The temperature dependent silica extinction coefficient is given approximately by the expression[114]: $k'' = a \cdot T + b$ where $a = 1.8 \cdot 10^{-2}$ and $b = 10 \cdot 10^{-5}$, and is related to the absorption coefficient by: $\alpha = \frac{4\pi k''}{\lambda} =$ (i.e. the e^{-1} penetration depth). The expression is valid in the temperature range of 25-1800 $^\circ C$. The optical and thermal properties are given in the table C.1. The strong increase in temperature during the illumination process can also lead to temperature levels, which are sufficient to induce evaporation of the silica from the surface, This effect has been observed during microsphere fabrication and has been discussed in chapter 5 in the context of modal coupling.

Due to this strong temperature dependence of the silica optical extinction coefficient, as well as the thermal isolation of the undercut SiO_2 disk, irradiation of silica disks on a silicon pillar, will cause melting of the silica disk along the periphery. In

Properties	Silica (Thermal Oxide)	Silicon
Melting Point	1710 $^{\circ}C$	1414 $^{\circ}C$
Boiling Point	2590 $^{\circ}C$	3173 $^{\circ}C$
Thermal Conductivity	150 $\frac{W}{mK}$	1.3 $\frac{W}{mK}$

Table C.1: The optical and thermal properties of silica and silicon.

addition to having a far weaker optical absorption at 10.6 microns, silicon is 100 times more thermally conductive than silica[115][114]. The silicon pillar therefore remains significantly cooler and physically unaffected throughout the silica reflow process, serving as a heat sink to the selectively absorbed optical power in the silica layer. Due to the melting of the periphery and the action of surface tension, the disk was observed to shrink and more significantly form a toroidally shaped cavity boundary, in width exceeding that of the initial silica disk. As the disk diameter shrinks, the effective cross-section available to absorb laser power decreases and shrinkage is observed to terminate. Beyond this point, continued laser treatment at the same intensity results in no observable change of the structure. The process is therefore self-quenching with the final diameter of the molten disk rim controlled by lithography and chemical etch steps. It should be noted that it is possible to interrupt the reflow prior to quenching thereby producing a toroid with a diameter intermediate to the initial disk diameter and terminal diameter. The irradiation parameters (amplitude, pulse shape and duration), were controlled using a function generator driving the CO_2 laser, and pulse durations were in the range of typically several tens of milliseconds. Comparison of the final toroidal cavity volume to the initial preforms shows, that for high intensity illumination a significant fraction of the silica is lost during the selective reflow, due to evaporation which has been mentioned in Chapter 4.

Figure C.3 shows a scanning electron micrograph of a reflown disk structure. The imaging reveal the high degree of symmetry of the structure. The cross-sectional area of the cavity is circular and the resulting cavity geometry therefore a torus, which

can be characterized by two parameters:

$$\textbf{Minor diameter} \ : \ d$$

$$\textbf{Principal diameter} \ : \ D$$

As silica is consumed to form the toroidal cross sectional area, the minor diameter is larger or equal to the thickness of the silica microdisk prior to reflow. Reduction of the toroidal cross-sectional area can therefore be achieved by using thinner thermal oxide layers in the disk processing as well as by reducing the amount of undercut and limiting the amount of silica undergoing the liquid state. However, the use of thinner oxides leads to shape deformed disk microcavities, due to relaxation of the compressive strain inherent to thermally oxidized silicon wafers. This leads to a silica disk which exhibits wave-like cavity boundaries, which can transfer into shape deformed toroids during the reflow process. In addition the decreased silica film thickness requires more optical power to induce melting. For the CO_2 laser and focusing optics used in this work, the minimum oxide thickness that could be molten was 500 nm.

In some cases deviations from the toroidal geometry were observed, in which the toroid cross-sectional area was elliptic, however in the large majority of the toroids used in this work, the action of surface tension causes formation of a circular cross sectional areas with low eccentricity.

C.2 Toroid dimensional control by preform design

Increased lithographic control over the toroid geometry can be achieved by suitable design of the silica disk preform. Due to the thermal runaway effect, the thickness of the preform is an important parameter determining the required flux of CO_2 laser illumination to initiate silica reflow and toroid formation. As noted above, for thin oxide layers the required flux is strongly increased, and thus by using a variable preform thickness profile, the temperature distribution of the silica in the laser illumination process can be controlled. For example, an annular preform (i.e., thicker at

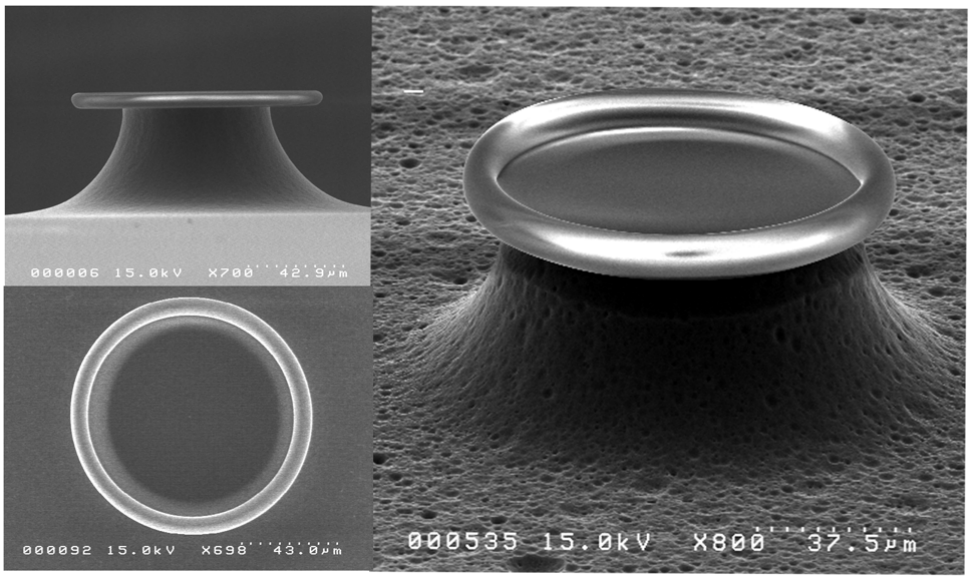

Figure C.3: SEM of a microdisk structure fabricated from a 1 micron thermal oxide. Due to the compressive strain induced by the thermal growth process used to oxidize silicon, the formed microdisk cavities exhibit warping around the perimeter due to strain relaxation. The effect increases as the pillar diameter is decreased and the oxide thickness is reduced. The inset shows the cavity geometry parameters; principal toroid diameter (D) and minor toroid diameter (d).

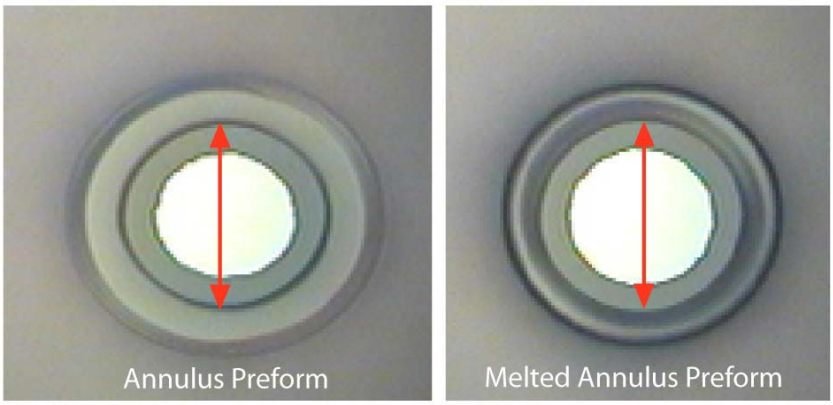

Figure C.4: An annular preform can be used to control the dimensions of the toroid. The left panel shows an annular preform prior to melting and the right panel shows the preform after irradiation. The CO_2 laser radiation selectively melts the thicker annulus perimeter, leaving the thinner interior disk unaffected.

the perimeter) will be preferentially heated at the perimeter, where the oxide thickness is large. We have found that not only does this mean that the melt initiates in the annulus, but significantly it is prevented from proceeding into thinner interior. The left panel of figure C.4 is an optical micrograph of an annular preform, featuring a thick rim at the perimeter (2 μm), and a thinner, interior disk (1 μm). In order to fabricate this structure two consecutive lithographic steps and buffered HF oxide etching were performed. The right panel in figure C.4 shows the structure after pulsed laser illumination. The outer annulus region preferentially melts and surface tension causes it to form a toroid. The process is observed to self-quench when the inner toroid diameter reaches the inner annulus diameter, and, significantly, prior to reaching the silicon pillar, The advantage of this fabrication technique is that the amount of material used to form the toroid as well as the inner diameter of the toroid micro-cavity can be accurately controlled by lithography. In addition, the supporting disk structure can be made very thin, which thereby increases the optical confinement of the modes within the toroidal periphery.